Calculation of the dielectric matrix of Si

1997 J. Phys.: Condens. Matter 9 1225

(http://iopscience.iop.org/0953-8984/9/6/009)

J. Phys.: Condens. Matter **9** (1997) 1225–1240. Printed in the UK PII: S0953-8984(97)78209-2

Calculation of the dielectric matrix of Si

M Ehrnsperger and H Bross
Sektion Physik der Universität München, D-80333 München, Germany

Received 30 September 1996

Abstract. The inverse microscopic dielectric matrix of crystalline silicon is evaluated within the time-dependent density-functional theory using one-electron energies and wave functions obtained by all-electron modified augmented-plane-wave band-structure calculations. Local fields are taken into account by inverting the dielectric matrix. The dependency of the exchange and correlation on the frequency and momentum is described using different approximations. We find that the polarization of the 2s and 2p core electrons changes the inverse dielectric function by up to 8%. In the long-wavelength limit our results for the region below 5 eV deviate from optical experiments by an almost constant energy shift, which is the same size as the band-gap error in local density approximation. Our results correspond with inelastic x-ray scattering spectroscopy measurements.

1. Introduction

In recent years the dielectric function (DEF) of silicon has been investigated extensively both experimentally and theoretically. Besides inelastic scattering and reflection experiments with electrons [1–4], the analysis of which is quite difficult [3, 5, 6], the dynamic structure factor was measured by means of inelastic x-ray scattering spectroscopy (IXSS) by Schülke and co-workers [7, 8]. For the first time non-diagonal elements of the inverse dielectric matrix (DEM) were also measured [9–11].

The long-wavelength limit of the DEF (see references in [12]) and its dependence on temperature [2, 13, 14] are obtained from optical experiments.

The first theoretical investigations of the DEF of silicon were based on rather simple models [15, 16], on the empirical pseudopotential method (EPM) [17–20] or on the empirical tight-binding (ETB) [21, 22] method. The recent *ab initio* investigations using pseudopotentials [23–30] or the orthogonalized-linear-combination-of-atomic-orbitals (OLCAO) method [31] are mostly concerned with specific cases ($\omega = 0$ and $\boldsymbol{q} = 0$) [23–25, 29] or with the long-wavelength limit [28, 30, 31] only. Exchange and correlation are taken into account in the random-phase approximation (RPA) [31] or local density approximation (LDA) [23–27] with gradient corrections (GC) [29] as well as self-energy corrections (GW) [28]. Local fields as introduced by Adler [32] are considered in almost all cited *ab initio* pseudopotential calculations but omitted in the OLCAO calculation. Only a small proportion of the IXSS data have been compared with calculations in a two-plasmon-band model [7, 33]. Still the following questions remain unsolved so far.

(i) How accurate is the dynamic structure factor obtained by the time-dependent density-functional theory (TDDFT) [34, 35] using different frequency- and momentum-dependent approximations of the exchange and correlation response kernel $f_{\mathrm{xc}\,\boldsymbol{K}\boldsymbol{K}'}(\boldsymbol{q}, \omega)$?

(ii) How strong is the core polarization, which is ignored in pseudopotential calculations?

0953-8984/97/061225+16$19.50

(iii) How important are the local field corrections, which need a great amount of CPU time?

2. Theory

The dielectric function is evaluated in the framework of the TDDFT, which leads to the following expression for the microscopic longitudinal dielectric function [36–40]:

$$\boldsymbol{\epsilon}(\boldsymbol{q},\omega) = \mathbf{1} - \mathbf{v}^{\mathrm{c}}(\boldsymbol{q},\omega)\boldsymbol{\chi}_{\mathrm{KS}}(\boldsymbol{q},\omega)\left[\mathbf{1} - \mathbf{f}_{\mathrm{xc}}(\boldsymbol{q},\omega)\boldsymbol{\chi}_{\mathrm{KS}}(\boldsymbol{q},\omega)\right]^{-1}. \tag{1}$$

The indices of the matrices are the reciprocal-lattice vectors ($\boldsymbol{K}$, $\boldsymbol{K}'$) and $\boldsymbol{q}$ is restricted to the first Brillouin zone. The Fourier transform of all matrices in (1) is defined by

$$A_{\boldsymbol{K}\boldsymbol{K}'}(\boldsymbol{q},\omega) = \frac{1}{V_{\mathrm{c}}}\int_{V_{\mathrm{c}}} \mathrm{d}^3 r \int \mathrm{d}^3 r' \, \exp[-\mathrm{i}(\boldsymbol{q}+\boldsymbol{K})\cdot\boldsymbol{r}] A(\boldsymbol{r},\boldsymbol{r}',\omega) \exp[\mathrm{i}(\boldsymbol{q}+\boldsymbol{K}')\cdot\boldsymbol{r}'] \tag{2}$$

where the integration with respect to $\boldsymbol{r}$ is taken over the Wigner–Seitz cell of volume V_{c} and the integration over $\boldsymbol{r}'$ extends over the volume of the crystal. $v^{\mathrm{c}}_{\boldsymbol{K}\boldsymbol{K}'}(\boldsymbol{q},\omega) = 4\pi e^2 \delta_{\boldsymbol{K}\boldsymbol{K}'}/\|\boldsymbol{q}+\boldsymbol{K}'\|^2$ is the Coulomb potential, and e the electron charge. The response function χ_{KS} of the non-interacting Kohn–Sham (KS) system is given by

$$\chi_{\mathrm{KS}\,\boldsymbol{K}\boldsymbol{K}'}(\boldsymbol{q},\omega) = \frac{2}{(2\pi)^3}\int \mathrm{d}^3 k \sum_{nn'} (f_{n\boldsymbol{k}} - f_{n'\boldsymbol{k}+\boldsymbol{q}}) \times \frac{\langle n\boldsymbol{k}|\exp[-\mathrm{i}(\boldsymbol{q}+\boldsymbol{K})\cdot\boldsymbol{r}]|n'\boldsymbol{k}+\boldsymbol{q}\rangle\langle n'\boldsymbol{k}+\boldsymbol{q}|\exp[\mathrm{i}(\boldsymbol{q}+\boldsymbol{K}')\cdot\boldsymbol{r}]|n\boldsymbol{k}\rangle}{E_{n\boldsymbol{k}} - E_{n'\boldsymbol{k}+\boldsymbol{q}} + \hbar(\omega+\mathrm{i}\eta)} \tag{3}$$

where the integration is taken over the first Brillouin zone. n and n' are band indices, $f_{n\boldsymbol{k}}$ is the occupation factor for the Bloch state $|n\boldsymbol{k}\rangle$ and η is a positive infinitesimal. The different approximations of the exchange–correlation response kernel f_{xc} used up to now are based on the hypothesis that the functional $f_{\mathrm{xc}}[\rho]$ depends on the density at $\boldsymbol{r}$, on an average density $\bar{\rho}$ and on the distance between $\boldsymbol{r}$ and $\boldsymbol{r}'$ only:

$$f_{\mathrm{xc}}[\rho](\boldsymbol{r},\boldsymbol{r}',t-t') = f_{\mathrm{xc}}(\rho(\boldsymbol{r}),\bar{\rho},|\boldsymbol{r}-\boldsymbol{r}'|,t-t'). \tag{4}$$

The right-hand side of (4) may be expressed by the Fourier transform

$$f_{\mathrm{xc}}(\rho(\boldsymbol{r}),\bar{\rho},|\boldsymbol{r}-\boldsymbol{r}'|,t-t') = \frac{1}{(2\pi)^3}\int \mathrm{d}^3 k \;\exp[\mathrm{i}\boldsymbol{k}\cdot(\boldsymbol{r}-\boldsymbol{r}')]\, f_{\mathrm{xc}}(\rho(\boldsymbol{r}),\bar{\rho},|\boldsymbol{k}|,t-t'). \tag{5}$$

Inserting (5) in (2) yields

$$f_{\mathrm{xc}\,\boldsymbol{K}\boldsymbol{K}'}(\boldsymbol{q},\omega) = \frac{1}{V_{\mathrm{c}}}\int_{V_{\mathrm{c}}} \mathrm{d}^3 r \;\exp[-\mathrm{i}(\boldsymbol{K}-\boldsymbol{K}')\cdot\boldsymbol{r}]\, f_{\mathrm{xc}}(\rho(\boldsymbol{r}),\bar{\rho},|\boldsymbol{q}+\boldsymbol{K}'|,\omega). \tag{6}$$

The following approximations for $f_{\mathrm{xc}}(\rho(\boldsymbol{r}),\bar{\rho},|\boldsymbol{k}|,\omega)$ have been discussed.

(a) $f_{\mathrm{xc}}(\rho(\boldsymbol{r}),\bar{\rho},|\boldsymbol{k}|,\omega) = 0$ in the RPA.

(b) Singhal and Callaway [36], Zangwill and Soven [37] and Bross *et al* [38] used

$$f_{\mathrm{xc}}(\rho(\boldsymbol{r}),\bar{\rho},|\boldsymbol{r}-\boldsymbol{r}'|,t-t') = \delta(\boldsymbol{r}-\boldsymbol{r}')\delta(t-t')\left.\frac{\partial^2 E_{\mathrm{xc}}}{\partial\rho^2}\right|_{\rho(\boldsymbol{r})} \tag{7}$$

which is local in space and instantaneous. In the sense of the X_α-approximation Singhal and Callaway used in the paper [36]

$$\left.\frac{\partial^2 E_{\mathrm{xc}}}{\partial\rho^2}\right|_{\rho(\boldsymbol{r})} \sim \rho^{-2/3}(\boldsymbol{r}).$$

(c) The expression used by Gross and Kohn [39]:

$$f_{\mathrm{xc}}(\rho(\boldsymbol{r}), \bar{\rho}, |\boldsymbol{r}-\boldsymbol{r}'|, \omega) = \delta(\boldsymbol{r}-\boldsymbol{r}')\, f_{\mathrm{xc}}^{\mathrm{h}}(\rho(\boldsymbol{r}), \boldsymbol{k}=0, \omega) \tag{8}$$

is still local in space.

(d) Dabrowski [40] took non-local parts of the exchange and correlation potential into account by assuming $f_{\mathrm{xc}}(\rho(\boldsymbol{r}), \bar{\rho}, |\boldsymbol{k}|, \omega) = f_{\mathrm{xc}}^{\mathrm{h}}(\rho(\boldsymbol{r}), |\boldsymbol{k}|, \omega)$.

Here $f_{\mathrm{xc}}^{\mathrm{h}}$ is the exchange–correlation kernel of the homogeneous electron gas. It is closely related to the function $G(\rho, |\boldsymbol{k}|, \omega)$:

$$f_{\mathrm{xc}}^{\mathrm{h}}(\rho, |\boldsymbol{k}|, \omega) = -\frac{4\pi e^2}{k^2} G(\rho, |\boldsymbol{k}|, \omega) \tag{9}$$

which is known as local field correction of the homogeneous electron gas. In the present paper we will not follow this nomenclature, to avoid confusion with the local field corrections in the sense of Adler [32]. A parametrization of $G(\rho, |\boldsymbol{k}|, \omega)$ was given by Dabrowski [40] coinciding with the limit $\omega = 0$ given by either Utsumi and Ichimaru [41] or Vashishta and Singwi [42] and with the limit $\omega = \infty$ given by Pathak and Vashishta [43]. Unless stated otherwise our calculations were performed with the proposal (d) using Dabrowski's [40] parametrization coinciding with the static limit of Utsumi and Ichimaru [41].

The dynamic structure factor $S(\boldsymbol{q}, \omega)$ is obtained via the fluctuation-dissipation theorem [44]:

$$S(\boldsymbol{q}+\boldsymbol{K}, \omega) = -\frac{(\boldsymbol{q}+\boldsymbol{K})^2}{4\pi^2 e^2 n} \operatorname{Im} \epsilon^{-1}_{\boldsymbol{K}\boldsymbol{K}}(\boldsymbol{q}, \omega) \tag{10}$$

showing that only the diagonal element of the inverse microscopic dielectric matrix is of interest. Here n is the density of the electrons.

3. Details of the numerical work

3.1. Band structure

The wave functions $|n\boldsymbol{k}\rangle$ and the energies $\epsilon_{n\boldsymbol{k}}$ were obtained in the MAPW formalism [45, 46] using a self-consistent potential evaluated by Bader [47]. This is a warped-muffin-tin potential in which multipole moments within the muffin-tin spheres are neglected. In order to avoid the difficulties caused by the incompleteness of the basis set described in [38] a relatively large Ritz *ansatz* was used: 9(6)†, 9(6) and 8(5) different radial functions $R_{sl}(r)$ were chosen for the angular momenta $l = 0$, 1 and 2, respectively, requiring that the logarithmic derivative $(1/R_{sl})(\mathrm{d}R_{sl}/\mathrm{d}r)$ on the surface of the muffin-tin sphere be either $+1$, 0, or -1. In this way radial functions R_{sl} covering the energy range up to 38(18) Ryd are taken into account. The number of plane waves was restricted by the requirement

$$|\boldsymbol{k}+\boldsymbol{K}|^2 \leqslant 27.5(2\pi/a)^2 \tag{11}$$

where a is the lattice constant. Depending on the value of the wave vector $\boldsymbol{k}$ this results in up to 169 plane waves and 285(221) different bands covering an energy range of up to 158(44) Ryd above the highest valence band. As we shall see in section 4.1 this set of Bloch functions is almost complete in a numerical sense. For the evaluation of the potential the smaller *ansatz* is sufficient since only occupied bands are needed. The importance of such a large *ansatz* has also been shown by Engel and Farid [27].

† The numbers in parentheses describe the *ansatz* used in Bader's [47] calculation of the self-consistent potential.

Correlation effects are taken into account in the self-consistent procedure using the local approximation of Hedin and Lundqvist [48] with the parameters given by Gunnarsson and Lundqvist [49]. All calculations were carried out for $a = 10.23$ au.

3.2. The matrix elements

Explicit expressions for $\langle n', \boldsymbol{k}+\boldsymbol{q} \,|\, \exp[\mathrm{i}(\boldsymbol{q}+\boldsymbol{K})\cdot\boldsymbol{r}\,]|\, n\boldsymbol{k}\rangle$ in the framework of the MAPW formalism are given elsewhere [50–52]. As these expressions consist of finite sums only, they can be evaluated with any desired accuracy. Without great effort it was possible to achieve an accuracy of seven digits.

3.3. Integration over the Brillouin zone

The concept of magic points was used as described in an earlier investigation [53]. Due to the partition of the Brillouin zone into small cubes the dielectric function shows some noise which can be reduced by convolution with suitably chosen Gaussians. After a convolution with 1.3 eV the maximum deviation between the functions calculated with 110 and 770 points in the irreducible wedge reaches 1.4%. 110 points are sufficient to explain experiments with a resolution up to 1.3 eV. Compared to a previous investigation of lithium [54] with the same scheme far fewer points are necessary since the bands do not cross the Fermi energy. As optical measurements show significantly higher resolution, we calculated the corresponding spectra using a mesh of 5740 points.

3.4. The rank of the dielectric matrix

The matrix operations according to (1) and (10) are performed with the set of 27 reciprocal-lattice vectors corresponding up to the third-nearest-neighbouring shell. Test calculations at $\boldsymbol{q} = (0.5\ 0\ 0)2\pi/a$ with 89 reciprocal-lattice vectors deviate by 2%. Engel and Farid [27] obtained similar results at $\boldsymbol{q} = (1\ 0\ 0)2\pi/a$, $\omega = 0$, using up to 140 reciprocal-lattice vectors.

In the long-wavelength limit local fields are found to be even more important [20]. As many as 59 reciprocal-lattice vectors are needed to keep the deviations from the results obtained with 89 vectors under 2%. This is in accord with the work of Baroni and Resta [23] who considered up to 181 reciprocal-lattice vectors at $\omega = 0$. For each value of $\boldsymbol{q}$ the calculation of the dielectric matrix needed about one week of CPU time on an HP 9000/735 workstation, depending on the direction of $\boldsymbol{q}$. In order to keep the computation time tolerable, the optical spectra are evaluated with 59 reciprocal-lattice vectors.

4. Results

4.1. Completeness of the Bloch functions

Accurate results for the dielectric function, especially for the real part, need an almost complete set of Bloch functions in the sense that the sum

$$\sigma_{n\boldsymbol{k}}(\boldsymbol{q}) = \sum_{n'} \langle n\boldsymbol{k}|\exp(\mathrm{i}\boldsymbol{q}\cdot\boldsymbol{r})|n'\boldsymbol{k}'\rangle\langle n'\boldsymbol{k}'|\exp(-\mathrm{i}\boldsymbol{q}\cdot\boldsymbol{r})|n\boldsymbol{k}\rangle \tag{12}$$

over all eigenstates obtained by solving the eigenvalue problem for a certain $\boldsymbol{k}$ differs only slightly from 1, at least for the occupied Bloch states. Due to the orthonormality of the Bloch states this requirement is identically fulfilled for $q = 0$. Using the $\boldsymbol{k}\cdot\boldsymbol{p}$ approximation one

finds that for small values of $|\boldsymbol{q}|$ the deviation $\sigma_{n\boldsymbol{k}}(\boldsymbol{q})-1$ behaves like $|\boldsymbol{q}|^2$ or even increases with a higher power of $\boldsymbol{q}$. The deviations 4×10^{-5} and 4.5×10^{-4} for $|\boldsymbol{q}|=0.5\times2\pi/a$ and $|\boldsymbol{q}|=1.5\times2\pi/a$ were found, respectively. An even larger *ansatz* consisting of 14, 14, 13 and 12 radial functions R_{sl} for the angular momenta 0, 1, 2 and 3, respectively, and about 244 plane waves leading to more than 580 bands reduced the deviation by a factor of 5. Equation (3) shows that $\sigma_{n\boldsymbol{k}}(\boldsymbol{q})-1$ is an upper limit for the numerical error in χ_{KS} caused by the incompleteness of the Ritz *ansatz*. As the precision of our final results is about 2% due to the error in the matrix inversion (see section 3.4), it is of no practical use to improve the completeness by a using larger Ritz *ansatz*.

Table 1. The f-sum rule. The ratios (right-hand side)/(left-hand side) of (13) or (14), respectively. The columns show different choices for f_{xc} described in section 2: RPA, LDA and f_{xc}(d) belong to proposals (a), (b) and (d), respectively.

	RPA(13)	LDA(13)	f_{xc}(d)(13)	RPA(14)
$\boldsymbol{q}=(0.5\ 0\ 0)2\pi/a$	1.0139	1.0136	1.0139	$1+4\times10^{-4}$
$\boldsymbol{q}=(1.2\ 1.2\ 1.2)2\pi/a$	0.9720	0.9745	0.9726	$1+7\times10^{-5}$

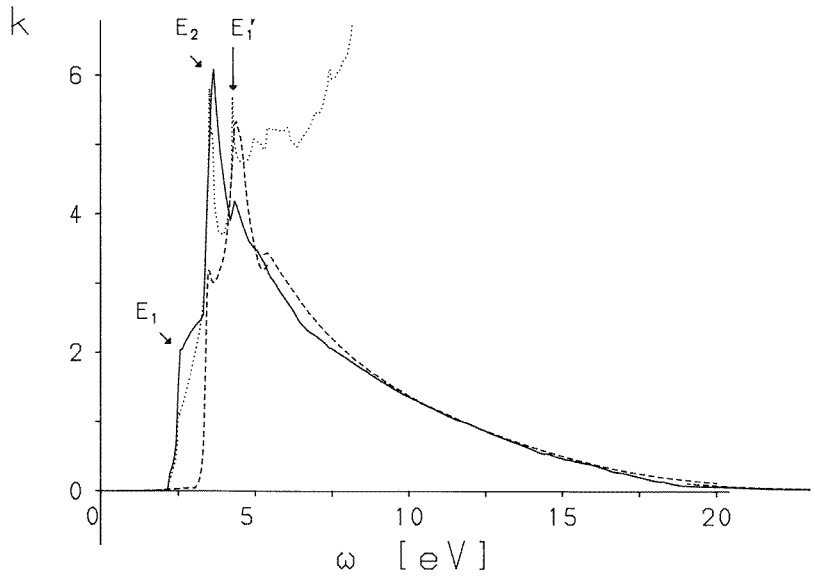

Figure 1. The imaginary part of the index of refraction $k=\mathrm{Im}\sqrt{1/\epsilon^{-1}_{00}}$. Solid line: theory; dashed line: experiment [14, 12]; dotted line: the joint density of states in arbitrary units.

4.2. Sum rules

As an additional test for the completeness of the *ansatz* as well as for the overall numerical accuracy of our calculations, two sum rules are investigated: the f-sum rule [44]:

$$\omega_{\mathrm{pl}}^2=-\int_{-\infty}^{\infty}\mathrm{Im}\,\epsilon^{-1}_{\boldsymbol{K}\boldsymbol{K}}(\boldsymbol{q},\omega)\,\omega\,\frac{\mathrm{d}\omega}{\pi} \tag{13}$$

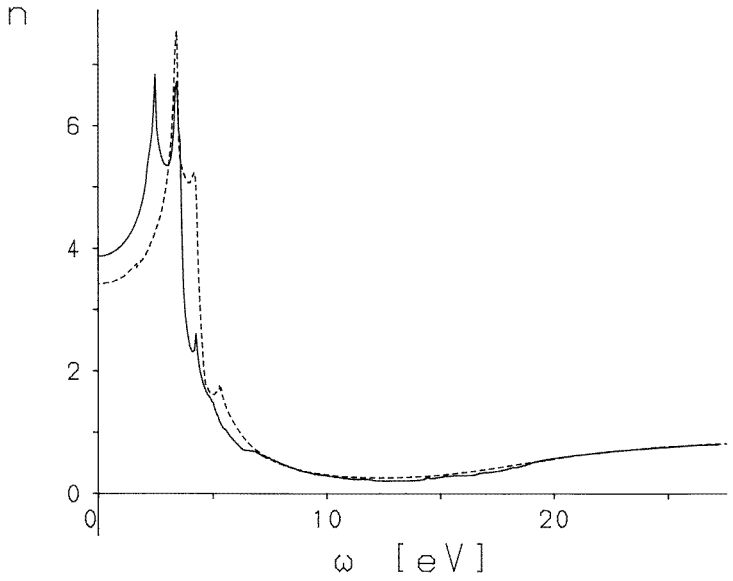

Figure 2. The real part of the index of refraction $n = \mathrm{Re}\sqrt{1/\epsilon^{-1}_{00}}$. Solid line: theory; dashed line: experiment [14, 12].

where $\omega_{\mathrm{pl}}^2 = 4\pi e^2 n/m$ is the plasma frequency of the valence electrons with average density n, and the Kramers–Kronig transform at zero frequency:

$$\mathrm{Re}\,\epsilon_{\boldsymbol{K}\boldsymbol{K}'}(\boldsymbol{q}, \omega = 0) = 1 + \int_{-\infty}^{\infty} \frac{\mathrm{Im}\,\epsilon_{\boldsymbol{K}\boldsymbol{K}'}(\boldsymbol{q}, \omega')}{\omega'} \frac{\mathrm{d}\omega'}{\pi}. \tag{14}$$

In order to test (14), $\mathrm{Re}\,\epsilon_{\boldsymbol{K}\boldsymbol{K}'}(\boldsymbol{q}, \omega = 0)$ is obtained with (1) and (3) directly. In the f-sum rule, the imaginary part of the DEF at high energies ($\simeq$100 Ryd) plays an important role through the factor ω in the numerator of the integral. In (14) the influence of these parts of the DEF is reduced through ω' in the denominator.

Table 1 shows that (14) is much better fulfilled in our calculation than (13). This supports the assumption that the deviations in (13) are caused mainly by small inaccuracies in the DEF at high energies.

Problems caused by non-local potentials as described in [30] do not appear in our work: there are no non-local potentials as long as we calculate within the RPA or LDA limit. Small non-local parts appear in the potential only if we use Dabrowski's proposal [40] for f_{xc} (see section 2). These parts affect the sum rule by less then 0.1%, which is below our numerical accuracy.

4.3. Core electron polarization

We calculated dielectric functions only up to 50 eV, which is smaller than the distance between the conduction band and the 2p core electrons (90 eV). Omission of the 2s and 2p electrons in the sum (3) leads to no change in $\mathrm{Im}\,\epsilon$ and small changes in $\mathrm{Re}\,\epsilon$ of about 0.1%†. However, a change of 8% in $\mathrm{Im}\,\epsilon^{-1}$ is found near some peaks of $\mathrm{Im}\,\epsilon^{-1}$, since the inverse dielectric function $\mathrm{Im}\,\epsilon^{-1}$ is very sensitive to small changes of $\mathrm{Re}\,\epsilon$ when both $\mathrm{Im}\,\epsilon$

† The test calculation was performed at $\boldsymbol{q} = (0.5\ 0\ 0)2\pi/a$; values are given in % of the maximum of the function.

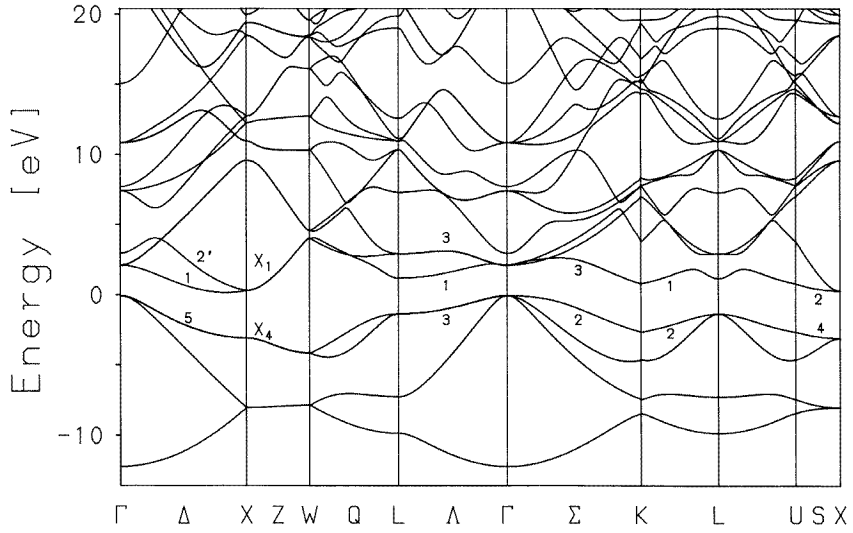

Figure 3. The band structure of silicon.

and $\mathrm{Re}\,\epsilon$ are small. Consequently the 2s and 2p electrons were taken into account in all calculations of $\mathrm{Im}\,\epsilon^{-1}$. On the other hand, the 1s core electrons are frozen in all calculations and omitted in the sum over n' in (12). Nevertheless the completeness (see section 4.1) is well satisfied.

Table 2. $\boldsymbol{k}$-vector-resolved joint densities of states obtained with 110 $\boldsymbol{k}$-points within the irreducible wedge for $\boldsymbol{q} = \boldsymbol{0}$. First to third column: the $\boldsymbol{k}$-point in units of $2\pi/a$. Fourth column: the contribution of the $\boldsymbol{k}$-point to the joint density of states in %.

$\omega = 2.52$ eV				$\omega = 3.54$ eV				$\omega = 4.28$ eV			
$\boldsymbol{k}$ $(2\pi/a)$			JDOS (%)	$\boldsymbol{k}$ $(2\pi/a)$			JDOS (%)	$\boldsymbol{k}$ $(2\pi/a)$			JDOS (%)
0.15	0.15	0.15	33.0	0.55	0.55	0.05	22.7	0.45	0.45	0.35	8.3
0.15	0.15	0.05	12.7	0.65	0.65	0.15	6.8	0.55	0.45	0.45	6.3
0.15	0.05	0.05	11.0	0.75	0.25	0.25	5.4	0.45	0.35	0.35	5.9
0.25	0.05	0.05	10.6	0.45	0.45	0.05	4.2	0.55	0.45	0.35	5.2
0.25	0.15	0.05	8.5	0.55	0.55	0.25	3.9	0.35	0.35	0.35	3.5
0.25	0.25	0.15	6.3	0.45	0.25	0.15	2.8	0.35	0.35	0.25	2.9
0.05	0.05	0.05	4.2	0.25	0.15	0.05	2.4	0.45	0.35	0.25	2.9
0.35	0.35	0.25	3.9	0.95	0.05	0.05	2.1	0.95	0.15	0.05	2.4
0.45	0.45	0.35	2.4	0.45	0.15	0.15	2.0	0.25	0.15	0.05	2.3
0.25	0.15	0.15	2.1	0.65	0.15	0.05	2.0	0.85	0.15	0.05	2.2
0.55	0.45	0.45	1.8	0.45	0.25	0.25	1.9	0.35	0.25	0.15	2.1
0.35	0.25	0.25	1.7	0.35	0.25	0.15	1.8	0.75	0.15	0.05	2.0
0.45	0.35	0.35	1.6	0.15	0.05	0.05	1.5	0.35	0.35	0.15	1.9
				0.25	0.15	0.15	1.4	0.45	0.35	0.15	1.7
				0.55	0.15	0.05	1.4	0.25	0.05	0.05	1.6
				0.75	0.15	0.05	1.4	0.65	0.05	0.05	1.6
				0.55	0.15	0.15	1.4	0.55	0.45	0.25	1.5
				0.45	0.25	0.05	1.4	0.15	0.15	0.05	1.5

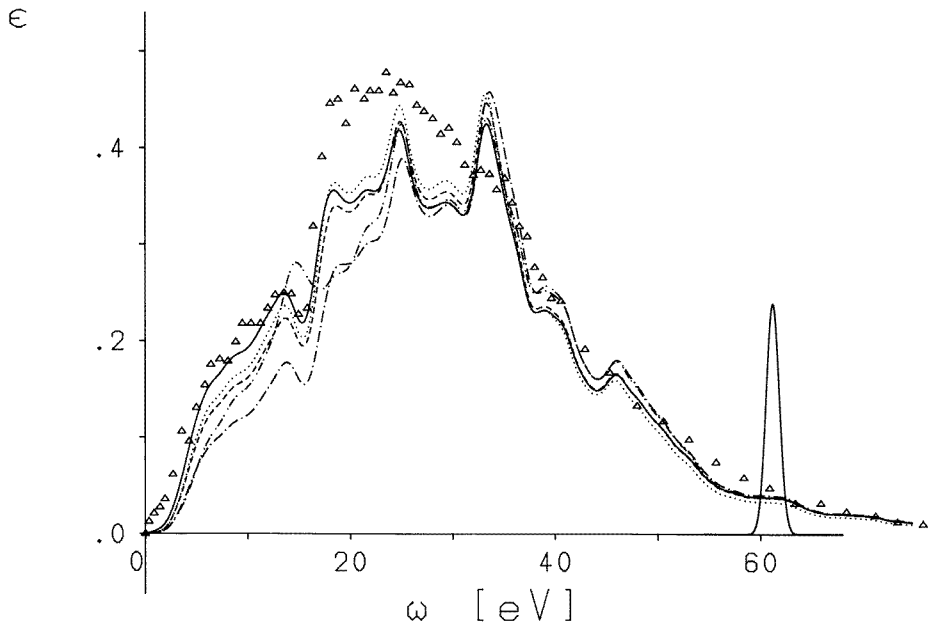

Figure 4. The inverse dielectric function for $q = 2.02 \times 2\pi/a$, $\boldsymbol{q}||[111]$, calculated with different approximations for f_{xc}. Solid line: the parametrization according to [40] and the static limit given by [41]. Dashed line: the parametrization according to [40] and the static limit given by [42]. Dotted line: the approximation proposed in [37]. Dashed–dotted line: $-\mathrm{Im}\,\epsilon_{\mathrm{RPA}}^{-1}$. Dashed–double-dotted line: $\mathrm{Im}\,\epsilon_{\mathrm{RPA}}/((\mathrm{Im}\,\epsilon_{\mathrm{RPA}})^2 + (\mathrm{Re}\,\epsilon_{\mathrm{RPA}})^2)$. Triangles: the values cited by Sturm, Schülke and Schmitz [7, 8]. The additional solid peak near 60 eV shows the resolution of 1.5 eV, which was used for the convolution.

4.4. The long-wavelength limit

Except for those for the joint density of states (JDOS), the calculations were performed with $\boldsymbol{q} = (0.025\ 0\ 0) \times 2\pi/a$, since the case where $q = 0$ cannot be directly treated by use of (1).

In figures 1 and 2 the theoretical and experimental spectra of the complex refraction index are compared. The curves closely coincide for frequencies above 5 eV. At smaller frequencies they are shifted against each other by the error in the band gap (0.92 eV). As the energies of the first three peaks or steps E_1, E_2 and E_1' coincide in the JDOS and $k = \mathrm{Im}\sqrt{1/\epsilon_{00}^{-1}}$, respectively, they can be assigned to transitions in $\boldsymbol{k}$-space. Both the $\boldsymbol{k}$-vector-resolved JDOS listed in table 2 and the band structure shown in figure 3 support this view.

The first peak at 2.52 eV arises primarily from the transition $\Lambda_3^v \rightarrow \Lambda_1^c$ and partly from the transition $\Delta_5^v \rightarrow \Delta_1^c$ between almost parallel bands (see figure 3). The second at 3.54 eV is attributed to the transitions $\Sigma_2^v \rightarrow \Sigma_3^c$ and to a smaller extent to the transitions $\mathrm{X}_4^v \rightarrow \mathrm{X}_1^c$. The third at 4.28 eV is located along the Λ direction ($\Lambda_3^v \rightarrow \Lambda_3^c$).

The same critical points are found by other authors (e.g. Adachi [55]) using a band structure obtained empirically by a fit to cyclotron resonance experiments and to optical measurements [56]. From this agreement we conclude that, within the energies of these critical points, the shape of the bands is reproduced correctly in the LDA: only the

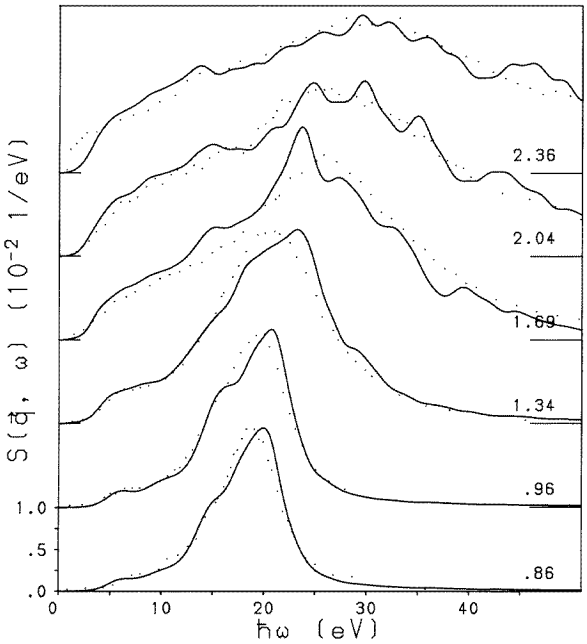

Figure 5. The dynamic structure factor $S(\boldsymbol{q}, \omega)$ in the [100] direction. Dots: values cited by Sturm, Schülke and Schmitz [7, 8]. Lines: calculated values convoluted with the experimental resolution. Right-hand side: $|\boldsymbol{q}|$ in units of $2\pi/a$.

conduction bands in the range between 0 and 5 eV above the valence bands must be shifted to correct the LDA.

Table 3. Experimental and theoretical values of $\epsilon_{\mathrm{M}}(\omega = 0) = \mathrm{Re}(1/\epsilon_{00}^{-1}(\boldsymbol{q} = 0, \omega = 0))$.

Present LDA, f_{XC} from reference [37]	14.7
Present, f_{XC} from reference [41]	15.0
Present, f_{XC} from reference [42]	14.7
Present RPA	14.0
LDA (reference [28])	13.5
LDA (reference [29])	12.7
RPA (reference [23])	12.04
GC (reference [29])	12.6
GW (reference [28])	11.2
Experiment (0 K, reference [57])	11.4

In table 3 the static value of the macroscopic dielectric constant obtained by different calculations and its experimental value are listed. The value calculated with f_{XC} from [37] is fully consistent with the LDA band structure. The other proposals for f_{XC} take some non-local effects into account, but show only a small deviation from the LDA result. The values of ϵ_{M} obtained by several pseudopotential calculations based on the LDA [28, 29] show better agreement with the experimental value, although our calculations use much more realistic wave functions. This should, however, not be taken too seriously, since the deviation between the pseudopotential LDA results [28] and [29], each of which was

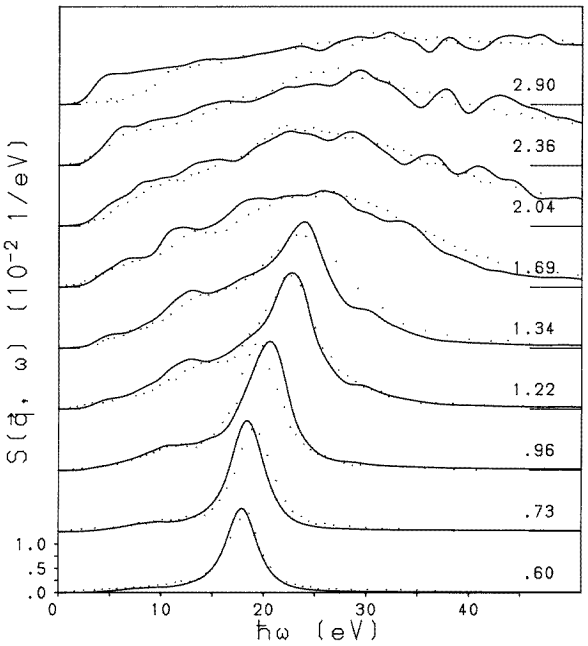

Figure 6. The dynamic structure factor $S(\boldsymbol{q}, \omega)$ in the [110] direction. Dots: values cited by Sturm, Schülke and Schmitz [7, 8]. Lines: calculated values convoluted with the experimental resolution. Right-hand side: $|\boldsymbol{q}|$ in units of $2\pi/a$.

calculated with a similarly large *ansatz*, is as large as the disagreement between these calculations and our result. We suspect that the deviations between the LDA results and the experiment are caused by the inadequacy of the LDA, which does not reproduce the band gap. This conclusion is supported by the fact that the result obtained within the GW approximation [28] agrees quite well with the experimental result.

4.5. The static dielectric matrix

In table 4 some relevant elements of the static dielectric matrix $\tilde{\epsilon}_{\boldsymbol{K}\boldsymbol{K}'}(\boldsymbol{q}) = (|\boldsymbol{q}+\boldsymbol{K}|/|\boldsymbol{q}+\boldsymbol{K}'|)\epsilon_{\boldsymbol{K}\boldsymbol{K}'}(\boldsymbol{q})$ up to the fifth shell are shown. The other elements can be calculated by means of the symmetry relations:

$$\tilde{\epsilon}_{\boldsymbol{K}\boldsymbol{K}'}(\boldsymbol{q}) = \tilde{\epsilon}_{\boldsymbol{K}'\boldsymbol{K}}(\boldsymbol{q}) \tag{15}$$

$$\tilde{\epsilon}_{\boldsymbol{\alpha}\boldsymbol{K}\boldsymbol{\alpha}\boldsymbol{K}'}(\boldsymbol{\alpha}\boldsymbol{q}) = \exp[\mathrm{i}\boldsymbol{\alpha}(\boldsymbol{K}-\boldsymbol{K}')\boldsymbol{\tau}_{\boldsymbol{\alpha}}]\,\tilde{\epsilon}_{\boldsymbol{K}\boldsymbol{K}'}(\boldsymbol{q}) \tag{16}$$

$$\lim_{\boldsymbol{q}\to 0,\boldsymbol{q}\|\boldsymbol{q}_1} \tilde{\epsilon}_{\boldsymbol{0}\boldsymbol{K}'}(\boldsymbol{q}) = \lim_{\boldsymbol{q}\to 0,\boldsymbol{q}\|\boldsymbol{q}_1} -\tilde{\epsilon}_{\boldsymbol{0}\boldsymbol{K}'}(-\boldsymbol{q}) \qquad (\boldsymbol{K}' \neq \boldsymbol{0}) \tag{17}$$

or must vanish due to these relations. $\lim_{\boldsymbol{q}\to 0}\tilde{\boldsymbol{\epsilon}}(\boldsymbol{q})$ depends on the direction of $\boldsymbol{q}$ if one of the pairs $(\boldsymbol{K}\boldsymbol{K}')$ vanishes. The matrix $\boldsymbol{\alpha}$ with the non primitive translation $\boldsymbol{\tau}_{\boldsymbol{\alpha}}$ describes a symmetry operation under which the crystal is invariant.

The calculations were performed with $\boldsymbol{q} = (0.025\ 0\ 0) \times 2\pi/a$. In table 4 the mean values of the matrix elements, which must be equal due to the symmetry requirements (15)–(17), are shown. The maximum deviation of 10% between that mean value and the calculated values for the non-diagonal elements and 1% for the diagonal elements of the matrix shows the quality of the approximation $\boldsymbol{q} \simeq \boldsymbol{0}$.

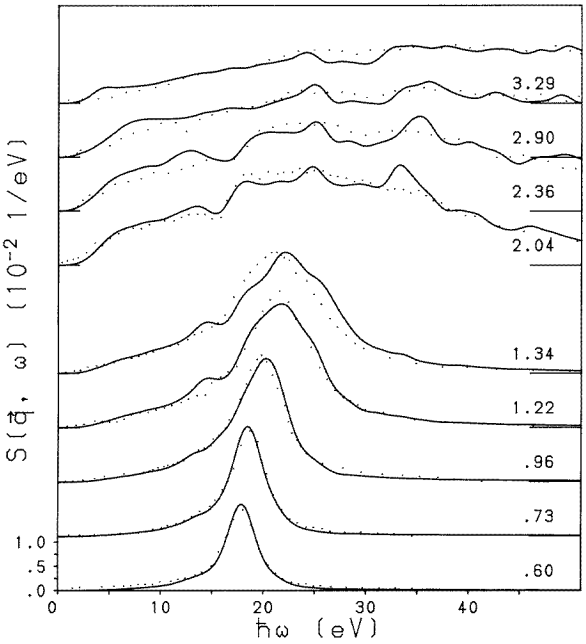

Figure 7. The dynamic structure factor $S(\boldsymbol{q},\omega)$ in the [111] direction. Dots: values cited by Sturm, Schülke and Schmitz [7, 8]. Lines: calculated values convoluted with the experimental resolution. Right-hand side: $|\boldsymbol{q}|$ in units of $2\pi/a$.

From table 4 we learn that the diagonal elements of the dielectric matrix are much larger than the non-diagonal elements. Let us now consider $\tilde{\epsilon} = \tilde{\epsilon}_{\mathrm{Diag}} + \tilde{\epsilon}_{\mathrm{NDiag}}$, $\tilde{\epsilon}_{\mathrm{Diag}}$ containing the diagonal elements of $\tilde{\epsilon}$ only. Then

$$\tilde{\epsilon}^{-1}_{\boldsymbol{K}\boldsymbol{K}'} \simeq (\tilde{\epsilon}_{\mathrm{Diag}})^{-1}_{\boldsymbol{K}\boldsymbol{K}}\delta_{\boldsymbol{K}\boldsymbol{K}'} - (\tilde{\epsilon}_{\mathrm{Diag}})^{-1}_{\boldsymbol{K}\boldsymbol{K}}\,\tilde{\epsilon}_{\mathrm{NDiag}\,\boldsymbol{K}\boldsymbol{K}'}\,(\tilde{\epsilon}_{\mathrm{Diag}})^{-1}_{\boldsymbol{K}'\boldsymbol{K}'} \tag{18}$$

holds approximately. This approximation gives a value of 15.5 for $1/\tilde{\epsilon}^{-1}_{\boldsymbol{0}\boldsymbol{0}}$, where the corresponding value obtained by inverting the matrix is 14.0. At first glance, the difference of 10% is surprising since the largest non-diagonal element of $\tilde{\epsilon}$ is only 3% of $\tilde{\epsilon}_{\boldsymbol{0}\boldsymbol{0}}$. A more sophisticated analysis, however, makes it clear that this difference is a consequence of the large number of the non-diagonal elements of the 59×59 matrix.

Using (18), known properties of ϵ can be transferred to ϵ^{-1}. In insulators and semiconductors like silicon, $\lim_{q\to 0}\epsilon_{\boldsymbol{0}\boldsymbol{K}'}(\boldsymbol{q}) \sim 1/|\boldsymbol{q}|$ holds for $\boldsymbol{K}' \neq 0$. From (18) it follows that

$$\begin{aligned}\lim_{\boldsymbol{q}\to 0}\epsilon^{-1}_{\boldsymbol{0}\boldsymbol{K}'}(\boldsymbol{q}) &= \lim_{\boldsymbol{q}\to 0}\frac{|\boldsymbol{q}+\boldsymbol{K}'|}{|\boldsymbol{q}|}\tilde{\epsilon}^{-1}_{\boldsymbol{0}\boldsymbol{K}'}(\boldsymbol{q}) \\ &\simeq \lim_{\boldsymbol{q}\to 0} -\frac{|\boldsymbol{q}+\boldsymbol{K}'|}{|\boldsymbol{q}|}\frac{\tilde{\epsilon}_{\boldsymbol{0}\boldsymbol{K}'}(\boldsymbol{q})}{\tilde{\epsilon}_{\boldsymbol{0}\boldsymbol{0}}(\boldsymbol{q})\tilde{\epsilon}_{\boldsymbol{K}'\boldsymbol{K}'}(\boldsymbol{q})} \sim \frac{1}{|\boldsymbol{q}|} \qquad \boldsymbol{K}' \neq 0.\end{aligned} \tag{19}$$

Seidl *et al* [58] pointed out that the non-diagonal elements of the static DEF are important for incorporating screened exchange in KS schemes.

Table 4. Elements of the matrix $\tilde{\epsilon}^{\mathrm{RPA}}_{\boldsymbol{K}\boldsymbol{K}'}(\boldsymbol{q}) = (|\boldsymbol{q}+\boldsymbol{K}|/|\boldsymbol{q}+\boldsymbol{K}'|)\epsilon^{\mathrm{RPA}}_{\boldsymbol{K}\boldsymbol{K}'}(\boldsymbol{q})$ in the limit $\boldsymbol{q}\to 0, \boldsymbol{q}||100$. First column: $\boldsymbol{K}$; first row: $\boldsymbol{K}'$; second row: $\tilde{\epsilon}^{\mathrm{RPA}}_{\boldsymbol{K}\boldsymbol{K}'}(\boldsymbol{q})$.

	000	111	220	022	311	131	222			
000	15.4646	−0.4665	0.1351	0.0015	0.1469	0.1085	0.1767			
	111	$11\bar{1}$	$1\bar{1}\bar{1}$	$\bar{1}\bar{1}\bar{1}$	200	$00\bar{2}$	220	$20\bar{2}$	$0\bar{2}\bar{2}$	311
111	1.7946	0.0195	−0.0167	−0.1917	0.1390	−0.0409	0.0915	0.0069	−0.0260	−0.0034
	$31\bar{1}$	$3\bar{1}\bar{1}$	$11\bar{3}$	$1\bar{1}\bar{3}$	$\bar{1}\bar{1}\bar{3}$	222	$22\bar{2}$	$2\bar{2}\bar{2}$	$\bar{2}\bar{2}\bar{2}$	
111	−0.0099	0.0003	0.0126	0.0018	−0.0066	−0.0818	−0.0254	0.0106	0.0070	
	200	020	$\bar{2}00$	022	311	131	$\bar{1}31$	$\bar{3}11$	222	$\bar{2}22$
200	1.6096	0.0087	−0.0043	−0.0123	−0.0719	0.0142	−0.0135	0.0052	0.0082	−0.0063
	220	202	$2\bar{2}0$	$0\bar{2}2$	$\bar{2}\bar{2}0$	311	$3\bar{1}1$	113	$1\bar{1}3$	$1\bar{3}1$
220	1.2462	−0.0121	0.0152	0.0047	−0.0225	0.0496	−0.0146	−0.0141	−0.0103	0.0009
	$\bar{1}\bar{1}3$	$\bar{1}3\bar{1}$	222	$2\bar{2}2$	$\bar{2}\bar{2}2$					
220	0.0004	−0.0055	0.0050	−0.0025	−0.0025					
	311	$31\bar{1}$	$3\bar{1}\bar{1}$	131	$13\bar{1}$	$11\bar{3}$	$1\bar{1}\bar{3}$	$\bar{1}31$	$\bar{1}3\bar{1}$	$\bar{1}\bar{1}\bar{3}$
311	1.1287	0.0011	0.0044	0.0005	0.0082	0.0013	−0.0073	−0.0013	0.0073	−0.0047
	$\bar{1}\bar{1}\bar{3}$	$\bar{3}11$	$\bar{3}1\bar{1}$	$\bar{3}\bar{1}\bar{1}$	222	$22\bar{2}$	$2\bar{2}\bar{2}$	$\bar{2}22$	$\bar{2}2\bar{2}$	$\bar{2}\bar{2}\bar{2}$
311	−0.0016	−0.0024	0.0001	−0.0041	0.0337	0.0094	−0.0069	0.0027	−0.0015	−0.0044
	222	$22\bar{2}$	$2\bar{2}\bar{2}$	$\bar{2}\bar{2}\bar{2}$						
222	1.1075	0.0125	−0.0027	−0.0062						

4.6. Comparison of several approximations for f_{xc}

Figure 4 shows the inverse dielectric function obtained from IXSS experiments [7, 8] and theoretical results derived with different approximations for f_{xc}.

Compared to ϵ_{RPA} all approximations of the functional f_{xc} improve the result at energies below 30 eV. The best agreement with the experiment is obtained with the static limit given in [41]. It agrees with the experiment at energies below 20 eV and between 35 and 70 eV. Compared to the much simpler local approximation [37] it reproduces the experiment somewhat better below 18 eV and slightly worse between 20 and 30 eV. Excitonic excitations at energies below 2 eV are not seen in the theory. Local fields show the largest effect ($\simeq$30%) at 15 eV. A similar result was found by Sturm *et al* [7] using a pseudopotential scheme. We conclude that the results of Josefsson and Smith [20], according to which local fields at higher $|\boldsymbol{q}| \simeq 2\pi/a$ are negligible in the [100] direction, cannot be generalized for the [111] direction.

4.7. Comparison with IXSS experiments

The dynamic structure factor of silicon along the principal directions has been examined extensively by Schülke and co-workers [7, 8] in a series of IXSS experiments. In figures 5–7 these measurements are compared with our results obtained for the same values of

transferred momentum. In order to correct for possible inaccuracies in the absolute scale of the experimental curves†, we divided them by the free parameter λ ranging from 1 to 1.3. No other free parameters were fitted. λ was used in figures 5–7 only.

The theoretical structure is quite close to the experimental results, even for higher transferred momenta and energies. This shows that, apart from the deviations near the band gap (see section 4.4), the band structure is reproduced correctly by the LDA, and that the *ansatz* is large enough for calculating even higher bands. The oscillations appearing in the theoretical spectra for $|\boldsymbol{q}| > 2 \times 2\pi/a$ and $\hbar\omega > 30\ eV$ are certainly not realistic. They do not disappear even when a larger *ansatz* is used in test calculations. We found similar oscillations in the case of lithium [54]. Since other numerical inadequacies can almost be excluded (see section 3), we suspect that small artefacts of the band structure at higher energies might be the origin.

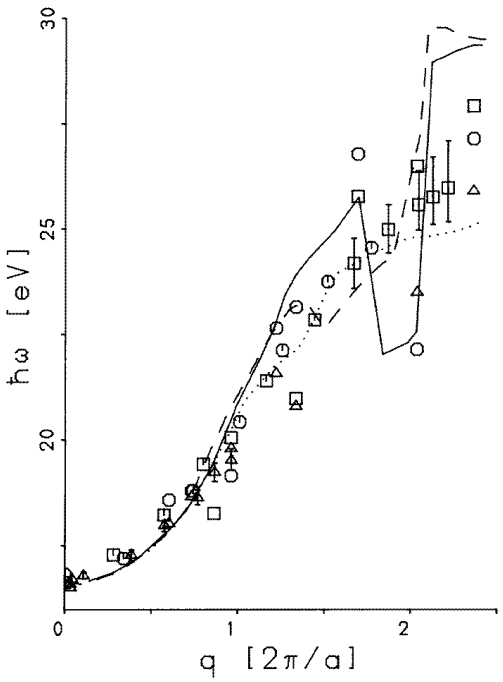

Figure 8. Peaks of the dynamic structure factor measured by various groups together with the values calculated in this work. [100] direction: dashed line: this work. Squares: reference [7, 8]. Primed squares and squares with error bars: reference [3]. [110] direction: solid line: this work. Circles: references [7, 8]. Primed circles: reference [3]. [111] direction: dotted line: this work. Triangles: references [7, 8]. Triangles with error bars: Reference [1].

In figure 8 the positions of all peaks observed by various groups [7, 8, 3, 1] are given in an ω–q plot together with the dispersion obtained from our theoretical results after a suitable convolution. Unrealistic oscillations above 30 eV were ignored for this purpose. At $q = 2.04 \times 2\pi/a$ in the [100] direction the theoretical curve in figure 5 shows two peaks of nearly the same height. In figure 8 the mean value of the two peak positions is plotted. The theoretical results coincide with the experimental values within the experimental accuracy. The latter is given by energy error bars, by the q-resolution

† Uncertainties in f_{xc} may be a reason as well.

estimated to be up to 10% [7], and by deviations between different groups.

For q below $1 \times 2\pi/a$ there is nearly no anisotropy and the dispersion is approximately quadratic. In the [110] direction the dispersion is negative between 1.7 and $1.8 \times 2\pi/a$, in agreement with the IXSS experiments [7, 8].

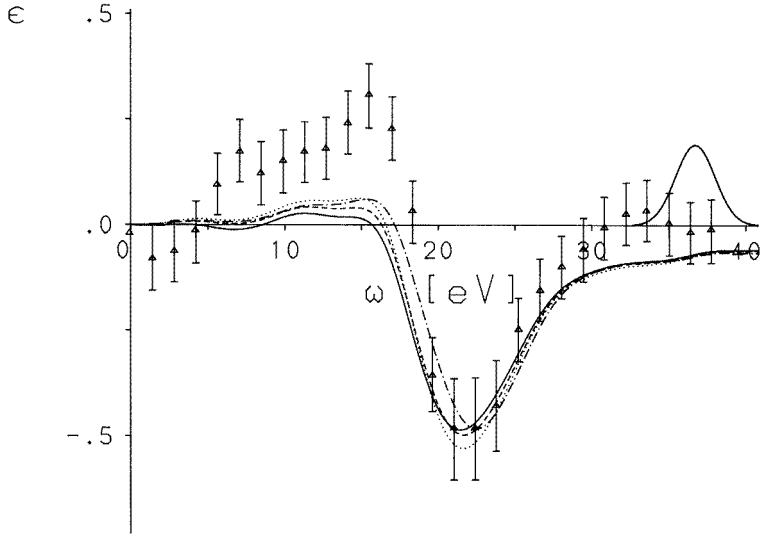

Figure 9. $-\mathrm{Im}\,\epsilon^{-1}_{\mathbf{0}\boldsymbol{K}}(\boldsymbol{q})$ for $\boldsymbol{q} = (0.9\ 0.3\ 0.3) \times 2\pi/a$ and $\boldsymbol{K} = (1\ 1\ 1) \times 2\pi/a$. Solid line: $-\mathrm{Im}\,\epsilon^{-1}_{\mathrm{UI}}$. Dashed line: $-\mathrm{Im}\,\epsilon^{-1}_{\mathrm{VS}}$. Dotted line: $-\mathrm{Im}\,\epsilon^{-1}_{\mathrm{local}}$. Dashed-dotted line: $-\mathrm{Im}\,\epsilon^{-1}_{\mathrm{RPA}}$. Triangles with error bars: values measured by Schülke and Kaprolat [9, 11]. The additional solid peak near 37 eV shows the resolution of 3 eV, which was used for convolution.

4.8. A non-diagonal element of the dielectric matrix

In figure 9 a non-diagonal element of the dielectric matrix is shown together with the experimental results [9, 11]. The peak near 22 eV coincides well, while at other energies the deviations are larger than the experimental error. The theoretical result depends only slightly on the chosen approximation for f_{xc}.

5. Conclusion

The dynamic structure factor is reproduced in the TDDFT within the experimental accuracy. The result depends only slightly on different approximations for f_{xc}. Polarization of the 2s and 2p core electrons changes the inverse dielectric matrix by up to 8%. In certain frequency regions and $\boldsymbol{q}$-directions the change of ϵ^{-1} caused by local field effects amounts to up to 30%.

Acknowledgments

The work was supported by the Bundesministerium für Forschung und Technologie via the grant 055WMAAI0 under the title: Theoretical Investigation of the Compton Profile and of

the Dynamic Structure Factor of some Crystalline Solids. We thank R Bader for providing the band-structure data and Professor W Schülke for the experimental data.

References

[1] Stiebling J and Raether H 1978 *Phys. Rev. Lett.* **40** 1293
[2] Daunois A and Aspnes D E 1978 *Phys. Rev.* B **18** 1824
[3] Chen C H, Meixner A E and Kincaid B M 1980 *Phys. Rev. Lett.* **44** 951
[4] Tougaard S and Kraaer J 1991 *Phys. Rev.* B **43** 1651
[5] Yubero F and Tougaard S 1992 *Phys. Rev.* B **46** 2486
[6] Yubero F, Tougaard S, Elizalde E and Sanz J M 1993 *Surf. Interface Anal.* **20** 719
[7] Sturm K, Schülke W and Schmitz J R 1992 *Phys. Rev. Lett.* **68** 228
[8] Schmitz J R 1991 *PhD Thesis* University of Dortmund
[9] Schülke W and Kaprolat A 1991 *Phys. Rev. Lett.* **67** 879
[10] Kaprolat A 1991 *PhD Thesis* University of Dortmund
[11] Kaprolat A and Schülke W 1993 *Z. Naturf.* a **48** 227
[12] Palik E D (ed) 1985 *Handbook of Optical Constants of Solids* (New York: Academic)
[13] Jellison G E Jr and Modine F A 1982 *J. Appl. Phys.* **53** 3745
[14] Lautenschlager P, Garriga M, Viña L and Cardona M 1987 *Phys. Rev.* B **36** 4821
[15] Fry J L 1969 *Phys. Rev.* **179** 892
[16] Milchev A 1978 *Phys. Status Solidi* b **90** 679
[17] Saravia L R and Brust D 1968 *Phys. Rev.* **171** 916
[18] Walter J P and Cohen M L 1972 *Phys. Rev.* B **5** 3101
[19] Daling R, van Haeringen W and Farid B 1991 *Phys. Rev.* B **44** 2952
[20] Josefsson T W and Smith A E 1993 *Aust. J. Phys.* **46** 635
[21] Moss D J, Ghahramani E, Sipe J E and van Driel H M 1990 *Phys. Rev.* B **41** 1542
[22] Graf M and Vogl P 1995 *Phys. Rev.* B **51** 4940
[23] Baroni S and Resta R 1986 *Phys. Rev.* B **33** 7017
[24] Baroni S, Giannozzi P and Testa A 1987 *Phys. Rev. Lett.* **58** 1861
[25] Giannozzi P, de Gironcoli S, Pavone P and Baroni S 1991 *Phys. Rev.* B **43** 7231
[26] Daling R, van Haeringen W and Farid B 1992 *Phys. Rev.* B **45** 8970
[27] Engel G E and Farid B 1992 *Phys. Rev.* B **46** 15 812
[28] Levine Z H and Allan D C 1991 *Phys. Rev.* B **43** 4187
[29] Dal Corso A, Baroni S and Resta R 1994 *Phys. Rev.* B **49** 5323
[30] Adolph B, Gavrilenko V I, Tenelsen K, Bechstedt F and Del Sole R 1996 *Phys. Rev.* B **53** 9797
[31] Huang M Z and Ching W Y 1993 *Phys. Rev.* B **47** 9449
[32] Adler S L 1962 *Phys. Rev.* **126** 413
[33] Sturm K and Schülke W 1992 *Phys. Rev.* B **46** 7193
[34] Runge E and Gross E K U 1984 *Phys. Rev. Lett.* **52** 997
[35] Gross E K U and Kohn W 1990 *Many-Fermion Systems (Advances in Quantum Chemistry 21)* ed S B Trickey (San Diego, CA: Academic) p 255
[36] Singhal S P and Callaway J 1976 *Phys. Rev.* B **14** 2347
[37] Zangwill A and Soven P 1980 *Phys. Rev.* A **21** 1561
[38] Bross H, Belhachemi O, Mekki B and Seoud A E H 1990 *J. Phys.: Condens. Matter* **2** 3919
[39] Gross E K U and Kohn W 1985 *Phys. Rev. Lett.* **55** 2850
[40] Dabrowski B 1986 *Phys. Rev.* B **34** 4989
[41] Utsumi K and Ichimaru S 1980 *Phys. Rev.* B **22** 5203
[42] Vashishta P and Singwi K S 1972 *Phys. Rev.* B **6** 875
[43] Pathak K N and Vashishta P 1973 *Phys. Rev.* B **7** 3649
[44] Pines D and Nozières P 1966 *The Theory of Quantum Liquids* vol 1 (New York: Benjamin)
[45] Bross H, Bohn G, Meister G, Schubö W and Stöhr H 1970 *Phys. Rev.* B **2** 3098
[46] Bross H and Eder R 1987 *Phys. Status Solidi* b **144** 175
[47] Bader R 1995 private communication
[48] Hedin L and Lundqvist B I 1971 *J. Phys. C: Solid State Phys.* **4** 206
[49] Gunnarsson O and Lundqvist B I 1976 *Phys. Rev.* B **13** 4274
[50] Seoud A E H 1983 *PhD Thesis* University of Munich
[51] Belhachemi O H 1986 *PhD Thesis* University of Munich

[52] Mekki B 1986 *PhD Thesis* University of Munich
[53] Bross H 1993 *Phys. Status Solidi* b **179** 429
[54] Bross H and Ehrnsperger M 1995 *Z. Phys.* B **97** 17
[55] Adachi S 1988 *Phys. Rev*. B **38** 12 966
[56] Cardona M and Pollak F H 1966 *Phys. Rev.* **142** 530
[57] Li H H 1980 *J. Phys. Chem. Ref. Data* **9** 561
[58] Seidl A, Görling A, Vogl P, Majewski J A and Levy M 1996 *Phys. Rev.* B **53** 3764